

We are IntechOpen, the world's leading publisher of Open Access books Built by scientists, for scientists

6,100

Open access books available

149,000

International authors and editors

185M

Downloads

Our authors are among the

154

Countries delivered to

TOP 1%

most cited scientists

12.2%

Contributors from top 500 universities



WEB OF SCIENCE™

Selection of our books indexed in the Book Citation Index
in Web of Science™ Core Collection (BKCI)

Interested in publishing with us?
Contact book.department@intechopen.com

Numbers displayed above are based on latest data collected.
For more information visit www.intechopen.com



Chapter

Three-Dimensional Microstrip Antennas for Uniform Phase Response or Wide-Angular Coverage GPS Applications

Ken G. Clark, Jim M. Tranquilla and Hussain M. Al-Rizzo

Abstract

In this chapter, three-dimensional microstrip antennas operating in the dominant TM_{10} mode of the L1 band at 1.57542 GHz are presented, which either provide uniform phase response and stable phase center, or wide angular beam coverage. A Finite-Difference Time-domain scheme has been developed and used to elucidate the interplay between the proposed antennas and several ground plane configurations. Experimental results are presented and compared to simulations to illustrate the impact of several 3-D geometries on the phase response, phase center, half power beam width, gain, and polarization purity. We report for the first-time novel three-dimensional microstrip antenna topologies for precise surveying applications by fostering a nearly uniform phase response when the 3D structure is bent by angles ranging from 15° to 30° **without significantly compromising the gain and polarization performance** of the equivalent flat patch antenna. The proposed antennas exhibit half-power-beamwidths up to 40 and 80% greater than the equivalent flat structure that can be realized if positioned downward and upward respectively, for bend angles above 45° accompanied with a variety of spatial coverage patterns to suit applications involving highly dynamic platforms.

Keywords: three-dimensional (3D) microstrip antennas, global positioning system, low-elevation pattern coverage, GPS tracking of sounding rockets and unmanned aerial vehicles, GPS aerospace applications

1. Introduction

The design requirements of a global positioning system (GPS) antenna rely on the application under consideration. A GPS user antenna is required to exhibit right-hand circular polarization (RHCP) and RHCP radiation pattern coverage from zenith down to five elevations for all azimuth angles to maintain tracking of the full visible satellite constellation during dynamic maneuvers [1–7]. An equally important, yet more challenging requirement is that the antenna must provide a virtually uniform phase response and stable phase center over the coverage region to satisfy precise positioning accuracy requirements [8–10].

Due to their light weight, size, low cost, and integration with printed-circuit boards, microstrip antennas offer an attractive solution to meet some of these design requirements. A considerable amount of research has been reported on the design of microstrip antennas for commercial GPS applications [11–16]. It is well known that conventional planar microstrip antennas suffer from reduced gain at low-elevation angles [7] which subsequently lead to loss of contact with GPS-received signals in particular when installed on highly-dynamic vehicles.

The demand for antennas that provide horizon-to-horizon coverage has risen considerably to keep pace with the recent stringent needs of modern GPS marine navigation and aerospace applications [16–21]. In this paper, we present three-dimensional microstrip antennas (3DMAs) for maritime GPS applications whereby pitch and roll amplitudes as high as 10–15° are encountered during adverse weather conditions [2]. Hence, the GPS antenna must provide coverage extending to negative elevation angles to compensate for vessel motion due to pitching and rolling [17–19]. Other potential applications for the antennas presented in this paper include tracking of unmanned aerial vehicles, space-borne vehicles, and sounding rockets where a key design objective is to provide a quasi-static isotropic radiation pattern to acquire the locally visible GPS satellites under the tumbling motion, during ascent trajectory and re-entry into the dense atmosphere [20, 21].

A few 3DMAs designs have been proposed to improve the radiation pattern of planar microstrip antennae in order to suit GPS applications involving highly-dynamic vehicles. A GPS manufacturer patented a downward 3DMAs design [5]. However, it should be noted that neither the dimensions were disclosed nor the claimed performance metrics were quantified in [5]. A corner truncated square patch, mounted on a pyramidal ground plane and partially enclosed within a flatly folded conducting wall was reported in [6] with a 3-dB Axial Ratio (AR) beamwidth of 130°. However, neither the phase response nor the phase center characteristics reported in [6]. In [7], we proposed a downward drooped square annular element resonating in the TM_{30} mode at 1.57542 GHz which revealed a complete upper hemispherical coverage with the pattern ripple being reduced to less than 2 dB. However, the antenna suffers from increased size (18.6 cm square annular element printed on a 4-mm thick substrate with a relative permittivity, $\epsilon_r = 2.2$). Moreover, the cross-polarized component became dominant by 1.5 dB near the horizon and the phase pattern displayed large variations in the elevation cut.

In contrast to the antennas reported in [5–7], this paper presents novel 3DMAs operating in the fundamental TM_{10} resonance mode, in which the ground plane and patch element are bent either downward or upward such that the corners or edges of the resonant cavity region fall away from the plane occupied by the patch. It should be emphasized that a fundamental understanding of the benefits and limitations of 3DMAs is still lacking. The key design parameters which influence the performance of the phase response of the far-field radiation pattern of 3DMAs such as bend angle, length of the flat portion, size of the ground plane, and substrate have not yet been reported in the literature.

In this paper, we present several downward and upward 3DMAs which are designed and characterized using a rigorous full-wave electromagnetic model and experimentally validated via measurements conducted inside an anechoic chamber. Our aim in investigating the 3DMAs is twofold: (i) to provide uniform phase response along with a stable phase center over the entire coverage region, and (ii) to symmetrically cover much of the upper hemisphere and to extend coverage to negative elevation angles so that the receiver can maintain lock with sufficient signal-to-noise ratio for all angles of the desired view. The first design goal is critical for minimizing

carrier and group delay variations in phase-tracking receivers. The second prevents occurrences of cycle slips and loss of lock to satellites, thereby reducing the Root-Mean-Square (RMS) error in position, velocity, acceleration, attitude, roll, pitch, and yaw of a moving platform [2, 18, 19].

The rest of the chapter is organized as follows. In Section 2, the geometries of the antennas under consideration are introduced. Section 3 summarizes the CPFDTD algorithm developed to perform the design and parametric studies along with experimental results to demonstrate its ability to correctly predict the resonant frequency and far-field radiation patterns. Section 4 introduces the antennas designed, constructed and tested for the control of the far-field radiation patterns with special emphasis on phase performance. Section 5 concludes the Chapter.

2. The design of the 3DMAs geometries

The reference Flat Microstrip Antenna (FMA), shown in **Figure 1(a)**, consists of a square copper patch, L_p in side length. The dielectric substrate has a thickness of h and the relative permittivity is denoted by ϵ_r . The patch is rotated by 45 with respect to the substrate layer.

Two types of 3DMAs are considered in this Chapter. The first is bent downward D3DMA shown in **Figure 1(b)**, the cross-sectional view of which is shown in **Figure 1(c)**. The second is the bent upward U3DMAs depicted in **Figure 2(a)**. The D3DMA is shown in **Figure 2(b)**. The side lengths of the ground plane and substrate are denoted by $L_g \times L_g$ and $L_s \times L_s$, respectively, where $L_g = L_s$. The D3DMA has a square flat top with a side length of L_f and the drooped angle with respect to the flat top side is denoted by ϕ . The length, L_p of the square patch is chosen to

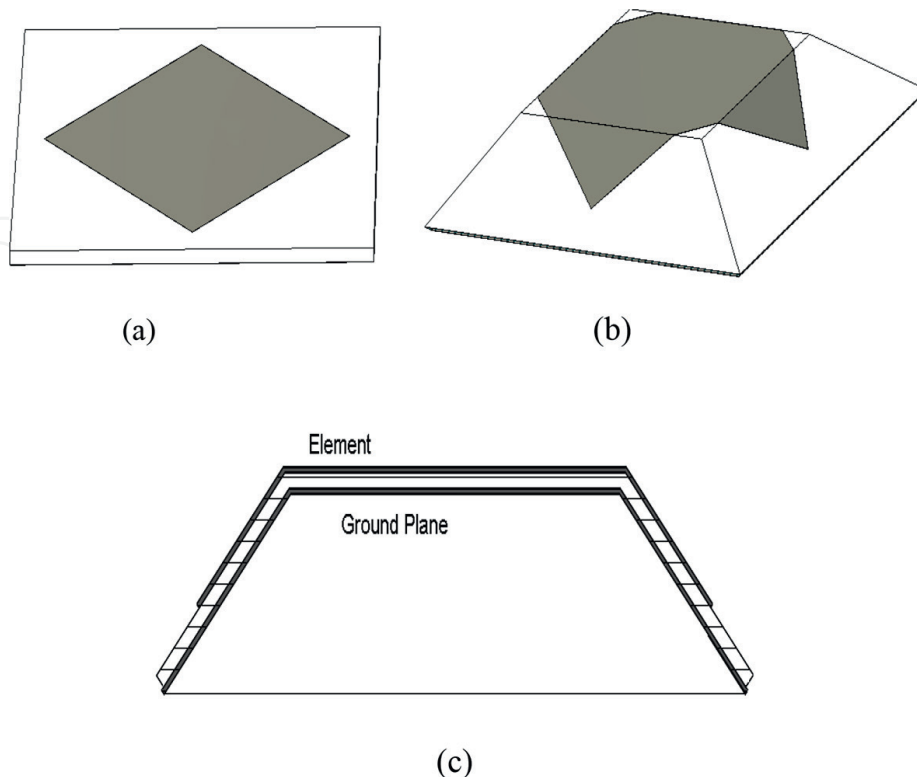


Figure 1.
(a) Reference FMA, (b) the D3DMA, (c) The resonant cavity.

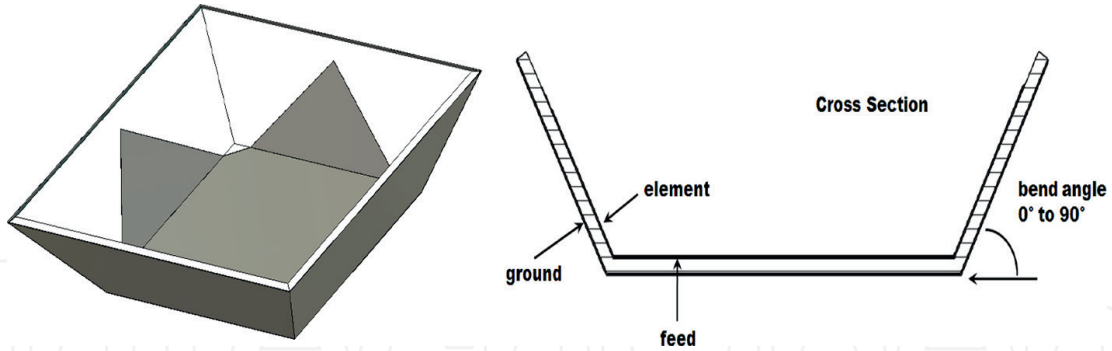


Figure 2.
(a) The U_3 DMAs, (b) The resonant cavity.

achieve the desired resonant frequency and bandwidth of the GPS L_1 carrier and varies according to ϕ , h , and ϵ_r . A 50Ω coaxial probe is used to feed all antennas presented in this Chapter, the inner conductor terminates on the patch.

3. Experimental validation of the CPFDTD modeling approach

The full-wave CPFDTD technique has been employed due to its flexibility for modeling complex structures. A versatile 3-D CPFDTD algorithm, combined with a thin-wire approximation, is implemented is developed with the formulation whereby different cell sizes can be chosen along the three orthogonal axes. Geometrical symmetry is implemented using the Neumann boundary condition. The input impedance of the antenna is obtained by exciting the coaxial cable port using a Gaussian pulse where the width and delay are determined from the resonant frequency and desired bandwidth. The appropriate electric and magnetic field components are integrated at the feed port to yield the voltage across and current flowing in the inner conductor which subsequently allows the computation of the input impedance in the frequency domain using Fourier transformation. To evaluate the magnitude and phase of the far-fields a sinusoidal signal where the frequency is chosen at the resonant mode of the structure and the simulations are ramped up to steady-state value over a number of cycles to ensure convergence to the desired accuracy.

The CPFDTD model is verified against the measured resonant frequency and ar-field radiation patterns. A simple prototype is simulated and constructed using only two edges bent down by an angle of 45° as shown in **Figure 3**.

These electromagnetic boundary conditions are enforced on the PEC conducting patch and ground plane which are not oriented along the Cartesian planes as follows. The electric and magnetic field components which are adjacent to the interface between two boundaries are updated using an integral approach applied to the fields that surround the contour of the appropriate cell [22]. This approach is better suited to conform to the 3-D surfaces under consideration to reduce numerical dispersion caused by traditional stair-step FDTD approximation.

As shown in **Figure 4**, the drooped surfaces are discretized using three different meshing schemes to suit a given bend angle. The vertical to horizontal mesh steps Δx and Δz are varied to conform to the drooping surface.

The measured resonant frequency is 1.55 GHz as compared to 1.575 GHz obtained from the CPFDT model. The measured phase response in the E -plane is displayed in **Figure 5**. The far-field patterns reveal asymmetry which is caused by the offset in the

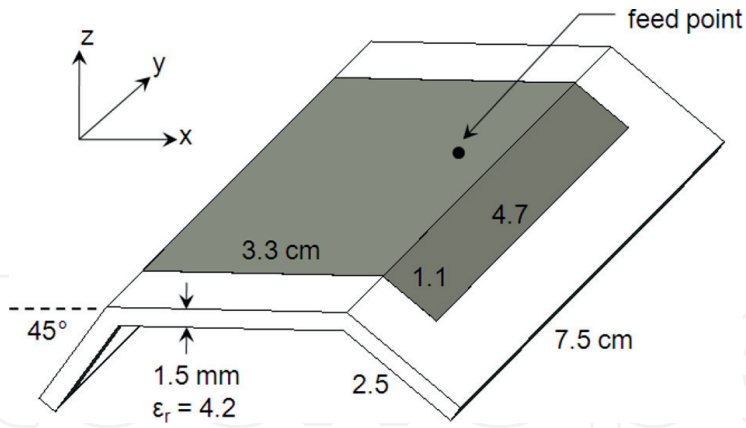


Figure 3.
 Prototype with two drooped edges; all dimensions are in cm.

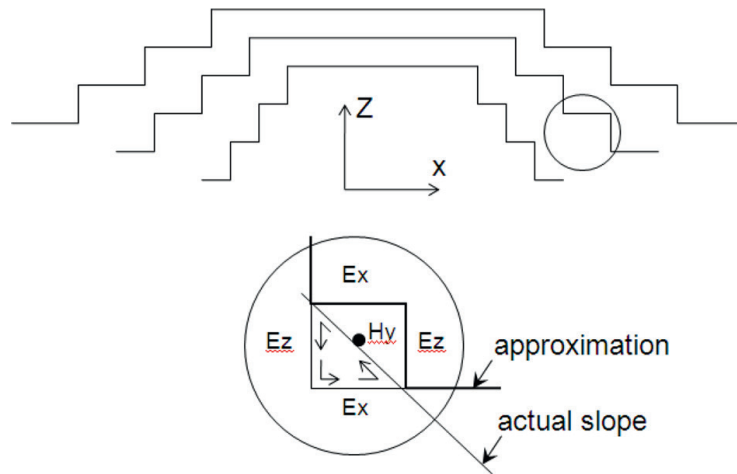


Figure 4.
 Approximation of shallow, intermediate, and steep surfaces.

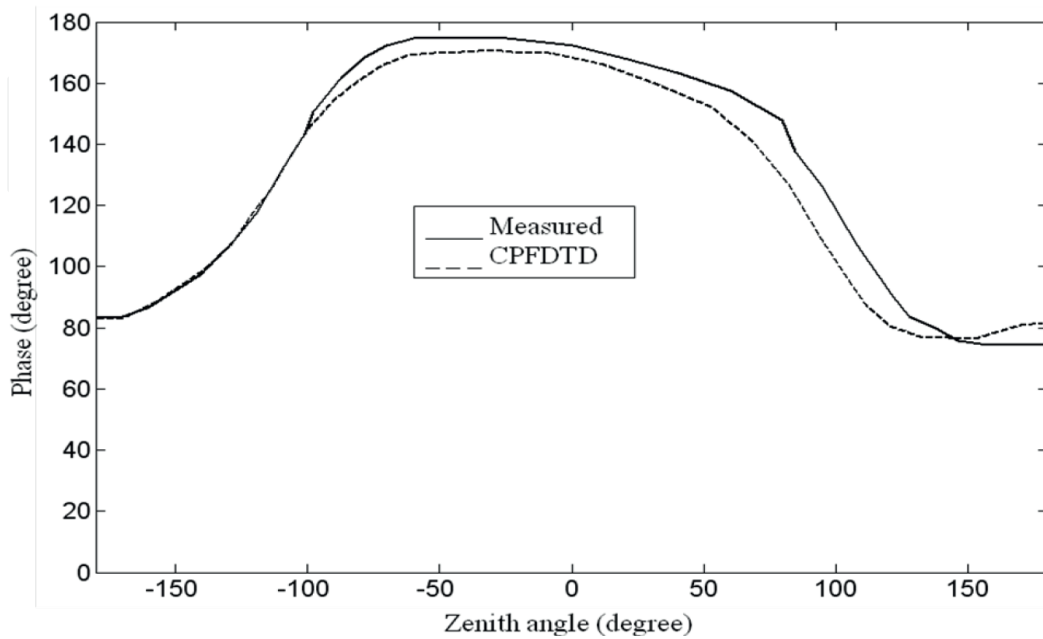


Figure 5.
 Measured and calculated phase pattern in the E-plane (x - z plane) for the antenna shown in **Figure 4**.

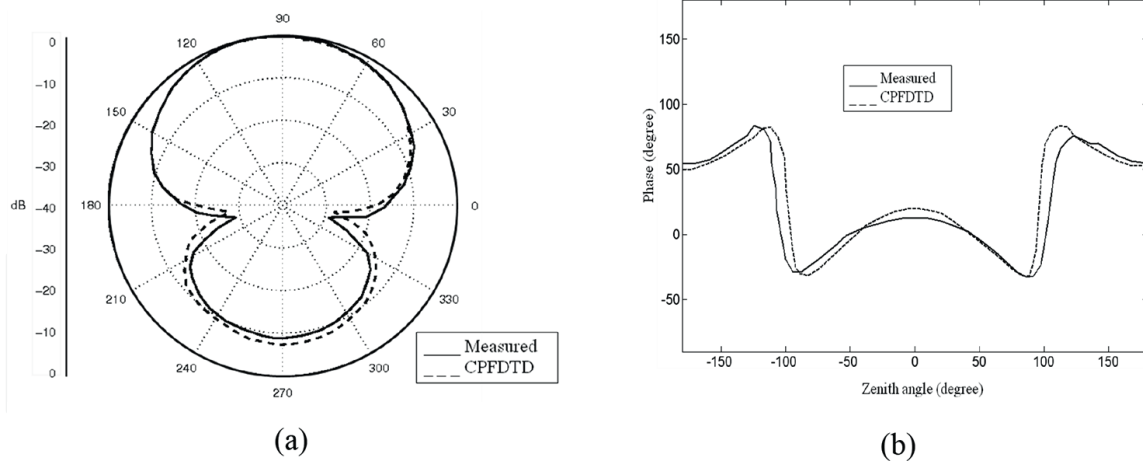


Figure 6. (a) Amplitude and (b) phase of the measured versus simulated far-field patterns in the H plane.

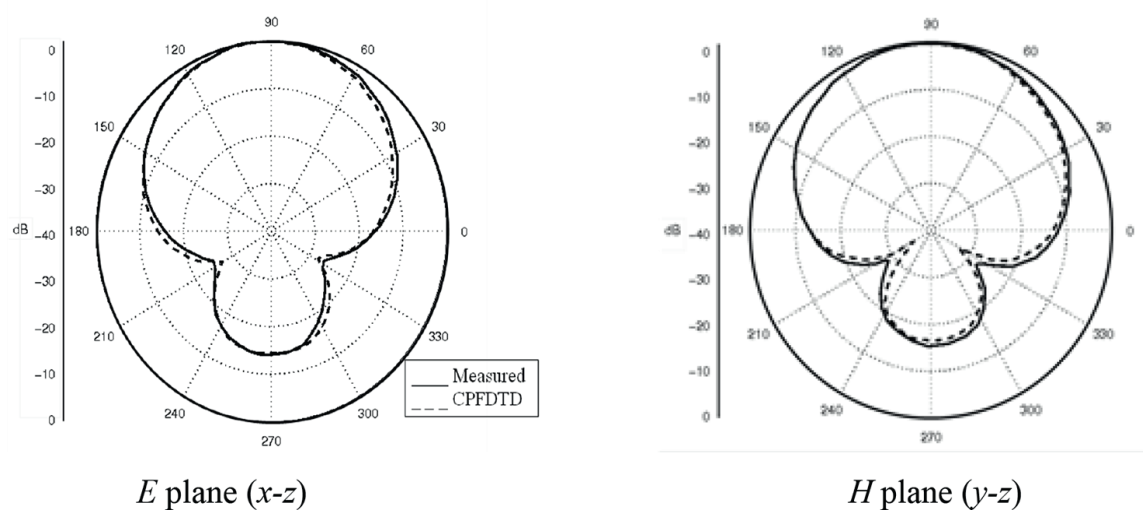


Figure 7. Measured and simulated elevation patterns for the 30° drooped antenna, $\epsilon_r = 2.2$.

antenna mount inside the anechoic chamber which is necessary in order to install the bends and cable on the antenna mount. For comparison, we referenced the calculated far-field patterns to the same offset origin. Results shown in **Figure 5** along with the amplitude and phase of the normalized H -plane patterns displayed in **Figure 6** show good agreement between measured and simulated results which validates our simulation approach.

Next, the bends are duplicated on the remaining two sides to arrive at the D3DMA geometry. We constructed a downward DMA to experimentally validate the final CPFDTD model. The prototype consists of a 62×62 mm patch, $L_f = 40$ mm, $\phi = 60^\circ$ printed on a substrate with $L_s = 100$ mm, $h = 1.5$ mm, and $\epsilon_r = 4.2$. As shown in **Figure 7**, excellent agreement is seen between the simulated and measured far-field radiation patterns in the E - and H -planes.

4. Design procedure and parametric study

In this section the impact of the bend angle, ϕ , length of the flat top, L_f , size of the ground plane, L_g , height, h , and the permittivity of the substrate, ϵ_r are analyzed to

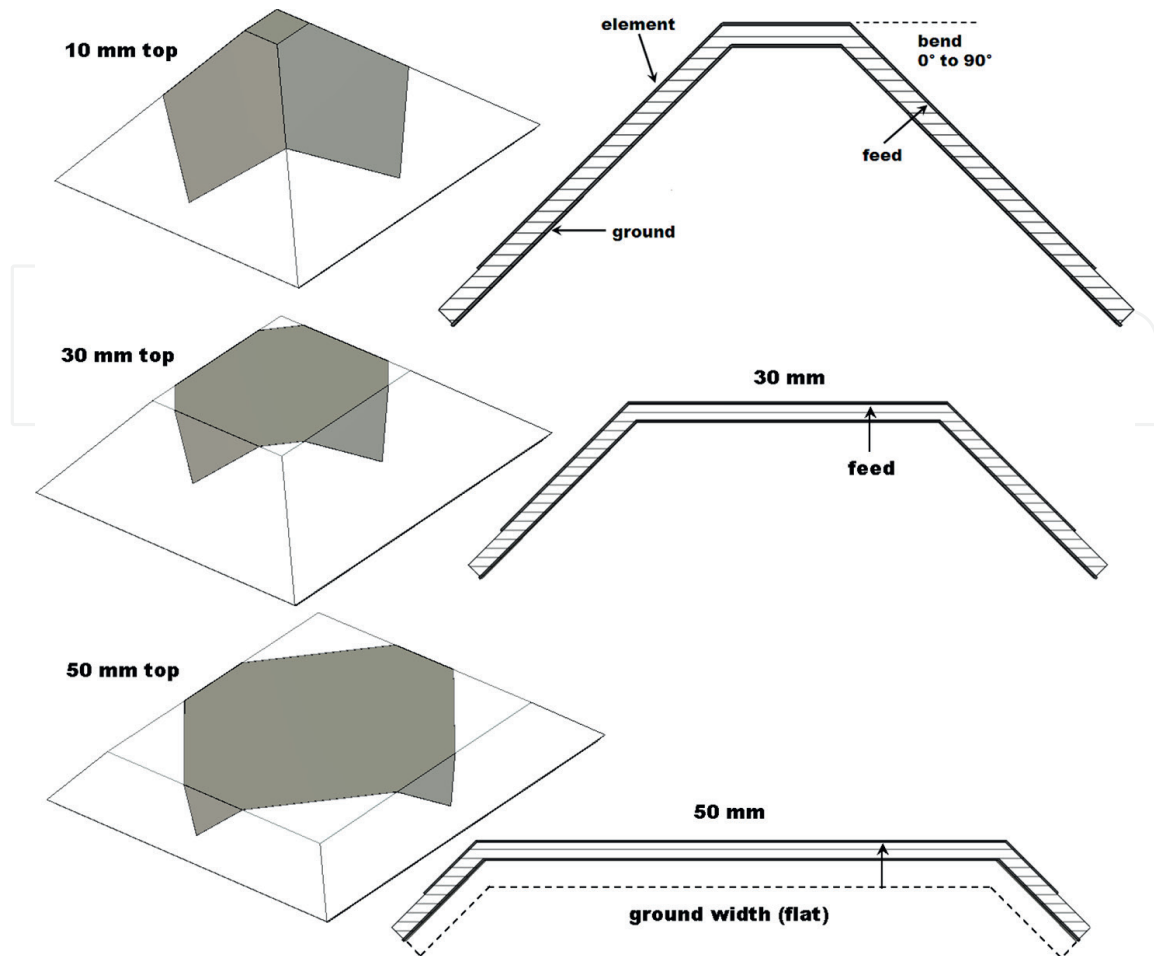


Figure 8.
 Structural variations: $L_f = 10, 30, \text{ and } 50 \text{ mm}$; $L_g = 85, 100, \text{ and } 120 \text{ mm}$.

evaluate their effects on the phase response, phase center, pattern coverage, gain, Half-Power-Beamwidths (HPBW), and polarization as compared to the equivalent FMA. The design process is complicated since several interacting parameters must be individually considered to meet the design objectives of the applications considered in this Chapter.

Figure 8 depicts the downward DMA configurations selected to perform the parametric study. A square patch is placed on three grounded substrates, $L_s = 85, 100, \text{ and } 120 \text{ mm}$. The substrates are bent at three positions in the center resulting square tops with dimensions of $L_f = 10, 30, \text{ and } 50 \text{ mm}$ as shown in **Figure 8**. Three substrates have been considered with $\epsilon_r = 2.2, 4.2, \text{ and } 10$.

4.1 Phase response

Some GSP antenna designs have been reported in the literature [2–9, 16, 17]. However, a close scrutiny of the literature revealed that the design focused mainly on the amplitude of the radiation patterns, expressed in terms of the realized gain. On the other hand, the phase response and phase center have been reported in [23] for a flat microstrip antenna installed on a metallic choke ring. It should be noted that depending on the angle of arrival of the satellite signals, the GPS antenna far-field phase response introduces phase distortion effect, hence, the phase response must be taken into consideration to accommodate sub-centimeter positioning accuracy.

To quantitatively assess the phase performance of the DMAs, the measured phase response is matched to an ideal hemisphere using a $5^\circ \times 5^\circ$ grid with equal solid angle

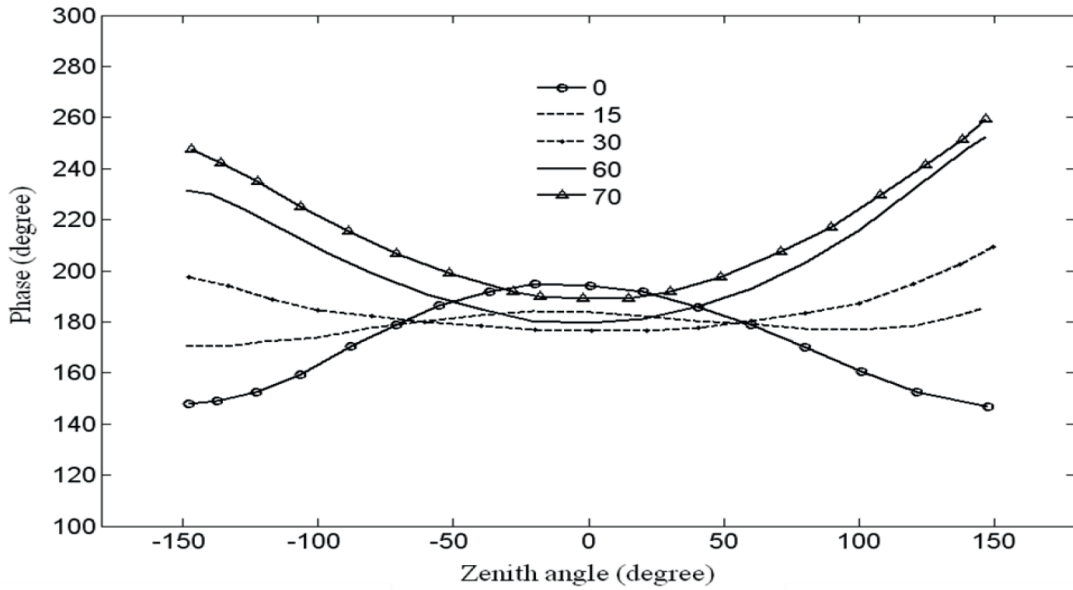


Figure 9.
Phase response for different bend angles, $L_g = 100$ mm, $L_f = 30$ mm, $\epsilon_r = 4.2$.

weighting. The phase center is next obtained by adjusting the center of the hemisphere by minimizing the RMS error between the 3-D measured and the theoretical hemispherical phase response pattern. The terms, “phase residual” or “phase error” are used to denote the difference between the measured and ideal phase in the 3-D far-field region. As a Figure-of-Merit, the RMS value of the phase error to characterize the stability of the phase center of the antennas introduced in this Chapter.

Elevation cuts of the phase pattern are presented in **Figure 9** for five downward DMAs with $L_g = 100$ mm, $L_f = 30$ mm, and $\epsilon_r = 4.2$. As shown in **Figure 9**, a noticeable improvement is seen in the below-horizon phase response for bend angles below 60° . As shown in **Figure 10**, it is clear that the phase response of the far-field patterns exhibits small variations above the horizon for bend angles ranging from 15° to 30° . Moreover, the RMS error in the upper hemisphere, as shown in **Figure 10**, shows little

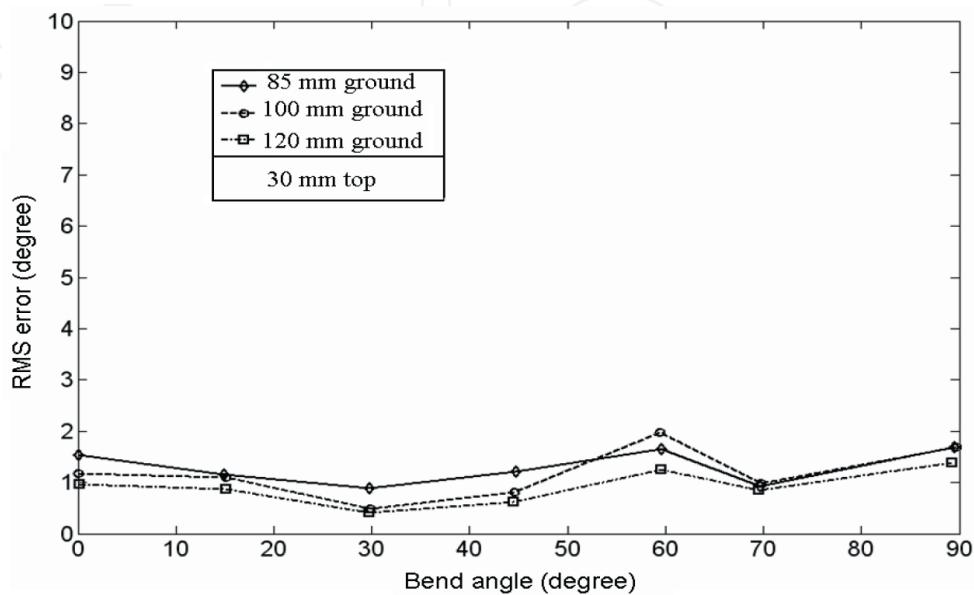


Figure 10.
RMS phase error using three ground planes, $\epsilon_r = 4.2$.

variations with bend angle or ground plane size. Hence, the antennas proposed in this Chapter provide uniform phase response and stable phase center over the entire upper hemisphere when constructed with a downward scheme for bend angles between 15° and 30° . These antennas are hence suitable for precise geodetic positioning since the phase difference of the antenna outputs corresponding to different view angles is uniform which will lead to reduced positioning errors.

4.2 Radiation patterns

The measured far-field radiation patterns are measured at the resonant frequency of the GPS L1 band inside an anechoic chamber. A sequence of the normalized patterns is presented in **Figure 11** for the E_θ component in the E -plane to illustrate the range of coverage patterns that could be achieved by varying ϕ , L_f , and L_g . **Figure 11** clearly demonstrates broader beam coverage for $\phi > 30^\circ$ and the wide range of fields of view that can be achieved in comparison to the FMA counterparts. As expected,

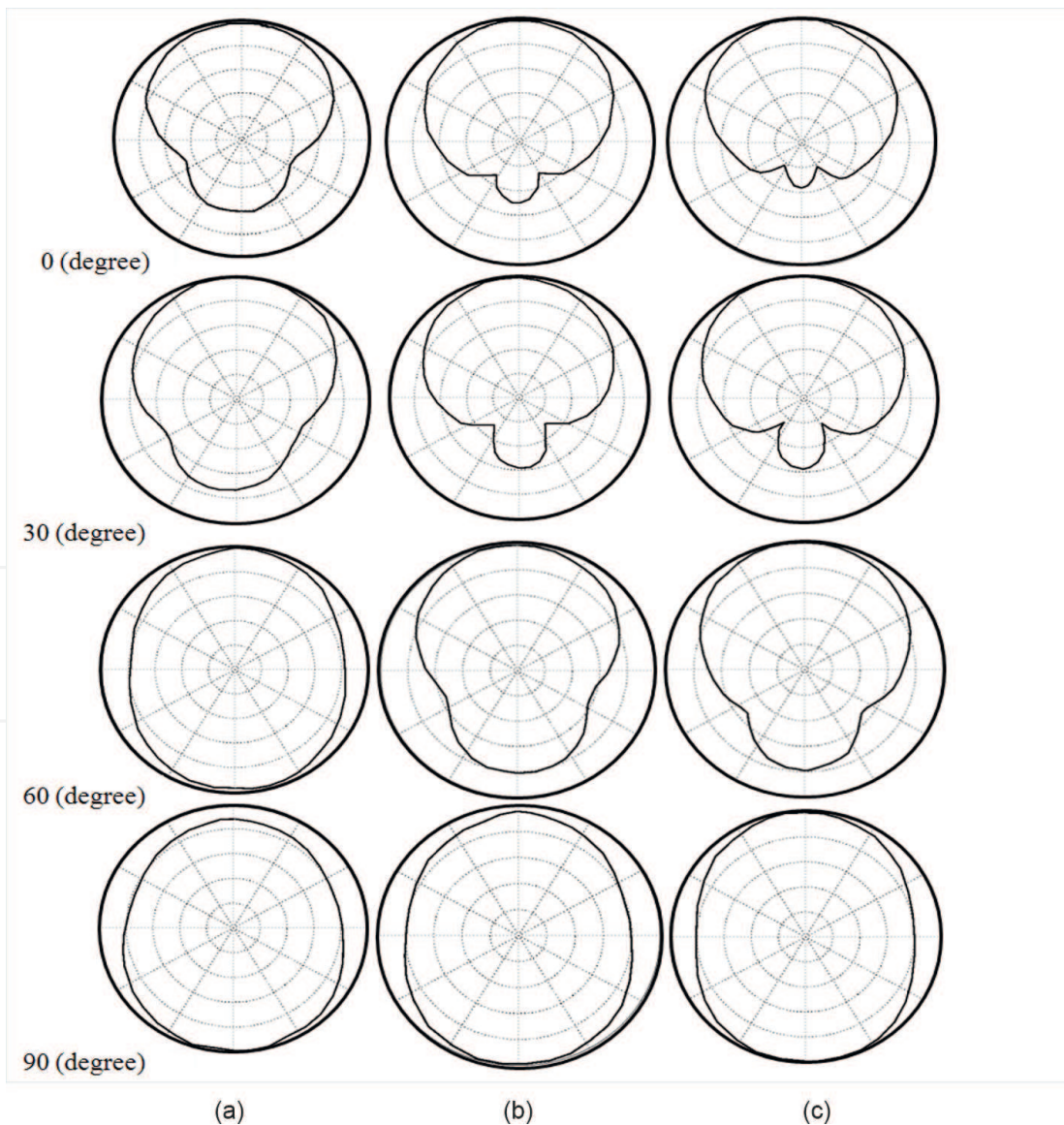


Figure 11. Elevation patterns versus the droop angle, ϕ (a) $L_g = 85$ mm, (b) $L_g = 100$ mm, and (c) $L_g = 120$ mm. E_θ component, $L_f = 30$ mm, $\epsilon_r = 2.2$, $h = 1.5$ mm. All patterns are normalized to 0 dB maximum, 10 dB/division.

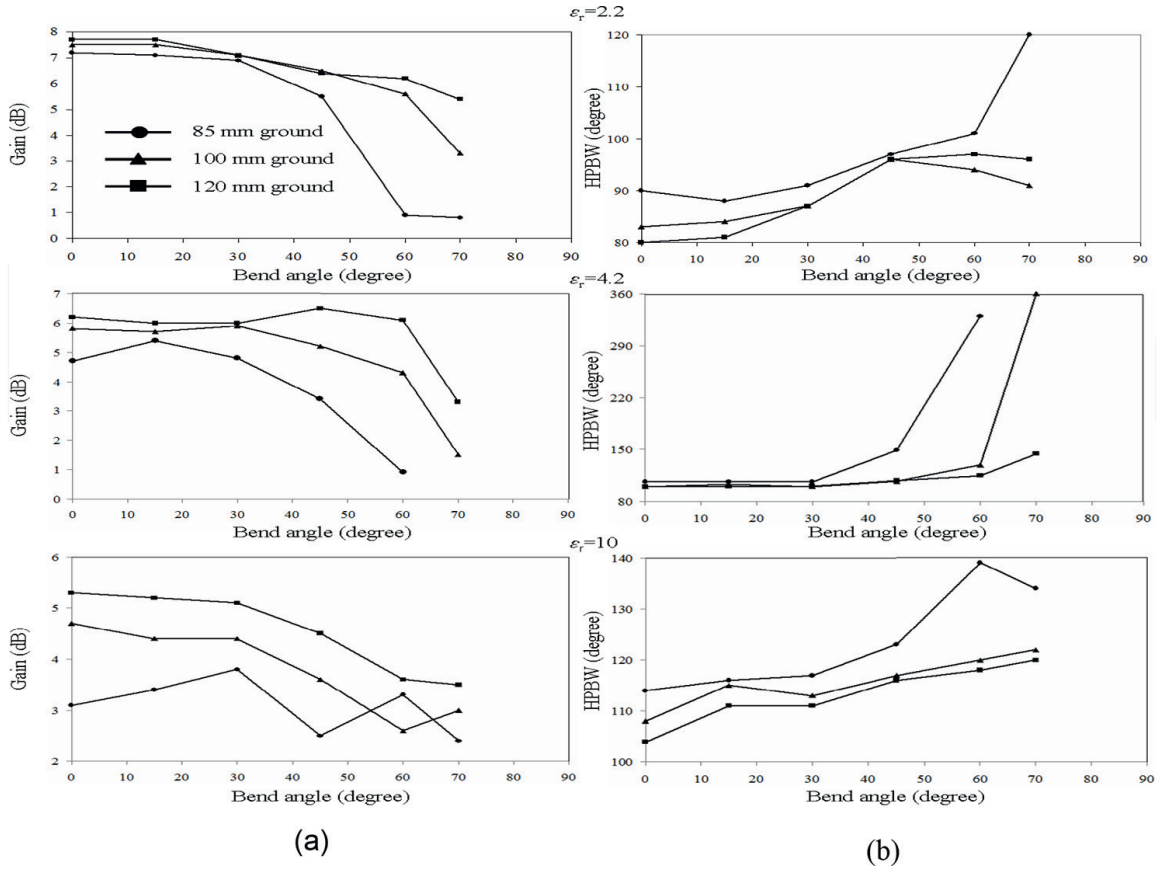


Figure 12. Gain and HPBW for the U₃DMAs versus bend angle, $L_f = 10$ mm, $L_g = 85, 100,$ and 120 mm, $\epsilon_r = 2.2, 4.2,$ and 10 the near-horizon gain roll off is -3.7 dB.

larger bend angles on small flat tops enhance coverage due to diffraction to the extent that the main lobe appears 180° from broadside when $\phi = 90^\circ$.

Among the three flat tops considered, results are displayed for the gain and HPBW for the case of $L_f = 10$ mm since it provided the best performance in terms of low-elevation angle coverage. **Figure 12** shows the results for the three ground planes

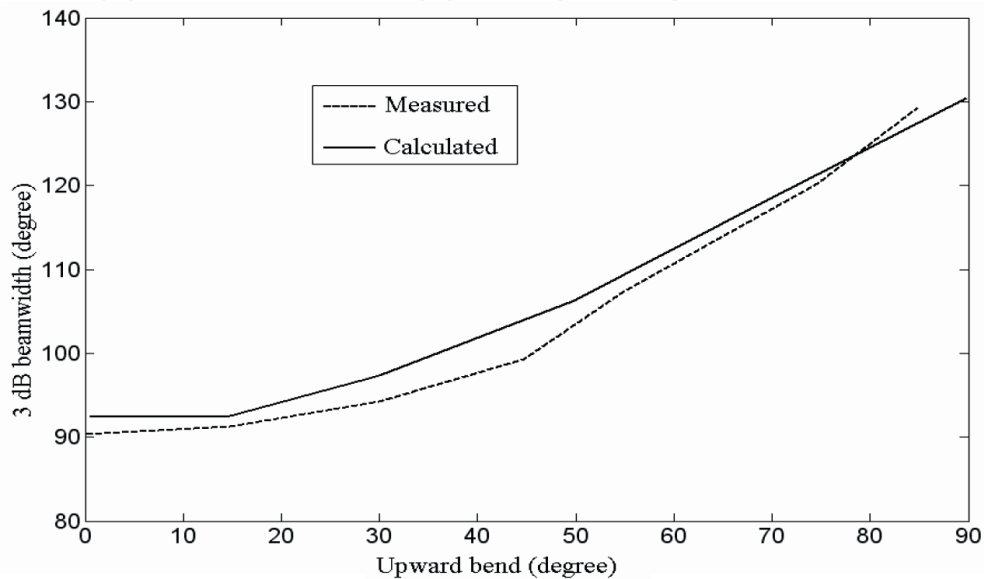


Figure 13. Measured and simulated HPBW of an adjustable upward DMA.

and substrates under consideration. For bend angles up to 30° , the pattern coverage is found to be not significantly different from the equivalent FMA, particularly for the larger ground planes and substrates with low ϵ_r . It is interesting to note that an increase of 40% is observed in the HPBW with respect to the equivalent FMA for the $\epsilon_r = 4.2$ substrate with $L_f = 10$ mm, $\phi = 45^\circ$, and $L_g = 85$ mm where the bore sight gain is 3.4 dB, and the near-horizon gain roll-off is -3.7 dB.

Next, the bore sight gain and HPBW are considered for the upward DMA. Simulations conducted for three bend locations: $L_f = 10, 30, 50$ mm; three substrates with $\epsilon_r = 2.2, 4.2, 10$; and three ground planes, $L_g = 85, 100, 120$ mm. Compared to the equivalent flat case, the U3DMA geometries considered provided a noticeable beam broadening at bend angles greater than 60° with up to a 60% increase in the HPBW as compared to the equivalent FMA.

To verify the simulation results, a U3DMA prototype with adjustable bend plates is constructed and tested to experimentally verify the results provided by our simulation model. No additional modifications to the topology of the antenna are made as ϕ

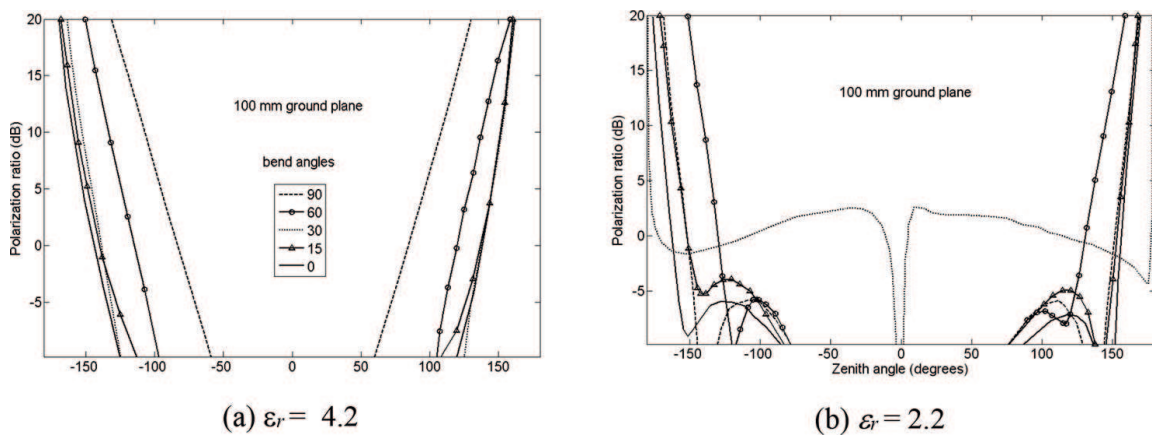


Figure 14. Polarization ratio for two different substrates, $L_g = 100$ mm, and five downward bend angles: (a) $\epsilon_r = 4.2$, (b) $\epsilon_r = 2.2$.

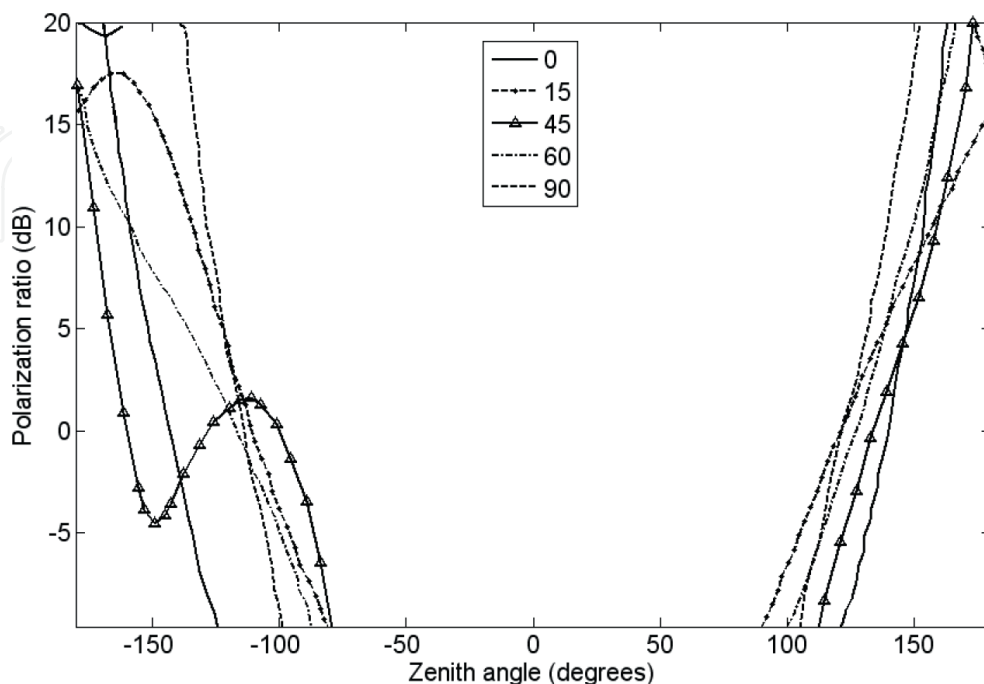


Figure 15. Axial ratio for different upward bend angles, $L_g = 100$ mm, $\epsilon_r = 2.2$.

changes. As can be observed from **Figure 13**, a good agreement is observed between simulated and measured HPBW.

4.3 Circular polarization purity

In this subsection, the polarization performance of the proposed antenna structures is investigated. The polarization performance near the horizon as shown in **Figure 14** is degraded with reference to the flat microstrip structure. As is the case for traditional flat microstrip antennas, the proposed antennas are not capable of rejecting multipath signals arising from reflection, diffraction, and scattering.

Similarly, the polarization ratio for the upward structures is shown in **Figure 15**. It is clear that the AR is better near the horizon when compared to downward bending. Below the horizon, the downward bending shows better performance. It can be concluded that in both cases, drooping the antenna increases the cross-polarization level near the horizon.

5. Conclusions

In this chapter, several 3DMA which provide a uniform phase response and stable phase center are presented for bend angles ranging from 15° to 30° , which are essential to achieve sub-centimeter accuracies in GPS receivers using carrier phase measurements. The excellent phase performance demonstrated for the moderately bent structures is of paramount importance if circumstances require bending the element but without a significant change in the radiation pattern of the FMA. It is interesting to note that this improvement is accompanied by a slight reduction in the bore sight gain and the polarization purity of the corresponding FMA. The same conclusion applies to the upward drooping, except for a sharp drop in gain observed for the 100 mm ground plane, 10 mm flat top, and the $\epsilon_r = 2.2$ substrate. The RMS phase error of the downward DMAs ranges from 0.42° to 4.3° for the three ground plane sizes, substrates, and flat portions considered for bend angles ranging from 0° to 90° . The corresponding RMS phase error for the upward DMAs ranges from 0.8° to 9.1° . For both the downward and upward DMAs, the RMS phase error decreases when the permittivity of the substrate increases and for increasing flat tops. In general, the downward DMA outperforms the upward DMA in terms of the RMS phase error performance.

On the other hand, higher bend angles allow improved GPS tracking performance for highly-dynamic marine navigation and space-borne applications. The length of the flat top, L_f and the bend angle, ϕ are found to be instrumental in the control of the radiation pattern. The upward DMA demonstrated a wider range of beam coverage compared to the FMA and downward counterparts. The half-power-beamwidth can be increased by up to 40 and 80% for the downward and upward bends, respectively, with respect to the traditional flat microstrip patch using the 10 mm flat top portion.

Finally, it is significant to stress that the design process of the 3DMA involves inevitable tradeoffs between achieving wide beam coverage, uniform phase response, gain, and polarization purity. If broad beam coverage is of precedence, some level of compromise will obviously be needed in regard to gain and multipath rejection, which requires excessive gain roll-off at low-elevation angles. Nonetheless, it turns out that the polarization purity of the proposed antenna has not significantly deteriorated since a maximum reduction of only 3 dB has been observed at the horizon in contrast to the flat microstrip structure.

IntechOpen

Author details


Ken G. Clark¹, Jim M. Tranquilla¹ and Hussain M. Al-Rizzo^{2*}

1 EMR Microwave Technology Corporation, Fredericton, Canada

2 Systems Engineering Department, Donaghey College of Science, Technology, Engineering, and Mathematics, University of Arkansas Little Rock, Little Rock, USA

*Address all correspondence to: hmalrizzo@ualr.edu

IntechOpen

© 2022 The Author(s). Licensee IntechOpen. This chapter is distributed under the terms of the Creative Commons Attribution License (<http://creativecommons.org/licenses/by/3.0>), which permits unrestricted use, distribution, and reproduction in any medium, provided the original work is properly cited. 

References

- [1] Scire-Scappuzzo F, Makarov SN. A low-multipath wideband gps antenna with cutoff or non-cutoff corrugated ground plane. *IEEE Transactions on Antennas and Propagation*. 2009;**57**(11):33-46
- [2] Lachapelle G, Casey M, Eaton RM, Kleusberg A, Tranquilla J, Wells D. GPS marine kinematic positioning accuracy and reliability. *The Canadian Surveyor*. 1987;**41**(2):143-172
- [3] Altshuler EE. Hemispherical Coverage Using a Double-Folded Monopole. *IEEE Transactions on Antennas and Propagation*. 1996;**44**(8):1112-1119
- [4] Zhang Y, Hui HT. A printed hemispherical helical antenna for GPS receivers. *IEEE Microwave and Wireless Components Letters*. 2005;**15**(1):10-12
- [5] Feller W. Three Dimensional Microstrip Patch Antenna. US Patent Publication No. 5,200,756. April 1993
- [6] Su CW, Huang SK, Lee CH. CP microstrip antenna with wide beamwidth for GPS band application. *Electronics Letters*. 2007;**43**(20):1062-1063
- [7] Al-Rizzo HM, Clark KG, Tranquilla JM, Adada RA, Elwi TA, Rucker D. Enhanced low-angle GPS coverage using solid and annular microstrip antennas on folded and drooped ground planes. *IEEE Transactions on Antennas and Propagation*. 2009;**AP-57**(11):3668-3672
- [8] Tranquilla JM, Best SR. A study of the quadrifilar helix antenna for global positioning systems (GPS) applications. *IEEE Transactions on Antennas and Propagation*. 1990;**38**:1545-1550
- [9] Shumaker PK, Ho CH, Smith KB. Printed half-wavelength quadrifilar helix antenna for gps marine applications. *Electronics Letters*. 1996;**32**:153-154
- [10] Best SR. Distance-measurement error associated with antenna phase-center displacement in time-reference radio positioning systems. *IEEE Antennas and Propagation Magazine*. 2004:13-22
- [11] Padros N, Ortigosa JI, Baker J, Iskander MF, Thornberg B. Comparative study of high-performance gps receiving antenna designs. *IEEE Transactions on Antennas and Propagation*. 1997;**45**(4):698-706
- [12] Boccia L, Amendola G, Massa GD. A dual frequency microstrip patch antenna for high-precision GPS applications. *IEEE Antennas and Wireless Propagation Letters*. 2004;**3**:157-160
- [13] Basilio LI, Williams JT, Jackson DR, Khayat MA. A comparative study of a new GPS reduced-surface-wave antenna. *IEEE Antennas and Wireless Propagation Letters*. 2005;**4**:233-236
- [14] Zhou Y, Koulouridis S, Kiziltas G, Volakis JL. A novel 1.5" quadruple antenna for tri-band GPS applications. *IEEE Antennas and Wireless Propagation Letters*. 2006;**5**:224-227
- [15] Basilio LI, Chen RL, Williams JT, Jackson DR. A new planar dual-band GPS antenna designed for reduced susceptibility to low-angle multipath. *IEEE Transactions on Antennas and Propagation*. 2007;**55**(8):2358-2366
- [16] Zhou Y, Chen C-C, Volakis JL. Single-fed circularly polarized antenna element with reduced coupling for GPS arrays.

IEEE Transactions on Antennas and Propagation. 2008;**56**(5):1469-1472

[17] Yaesh I, Prielm B. Design of leveling loop for marine navigation system. IEEE Transactions on Aerospace and Electronic Systems. 1993;**29**(2):599-604

[18] Lachapelle G, Cannon ME, Lu G, Loncarevic B. Ship borne GPS attitude determination during MMST-93. IEEE Journal of Oceanic Engineering. 1996;**21**(1):100-105

[19] Lu G, Cannon ME, Lachapelle G. Attitude determination using dedicated and nondedicated multiantenna GPS sensors. IEEE Transactions on Aerospace and Electronic Systems. 1994;**30**(4):1053-1058

[20] Bull B, Oiehl J, Montenbruck O, Markgraf M. Flight performance evaluation of three GPS receivers for sounding rocket tracking. National Technical Meeting Proceeding, ION GPS, Integrating Technology, January 28-30, 2002, San Diego, California. 2002

[21] Montenbruck O, Markgraf M, Hassenpflug F. Pre-flight Assessment of a Dual Blade Antenna System for GPS Tracking of Sounding Rocket. DLR-GSOC TN 01-03. Oberpfaffenhofen: Deutsches Zentrum für Luft- und Raumfahrt; 2001

[22] Jurgens TG, Taflove A, Umashankar KR, Moore TG. Finite-difference time-domain modeling of curved surfaces. IEEE Transactions on Antennas and Propagation. 1992;**AP-40**:357-366

[23] Tranquilla JM, Carr JP, Al-Rizzo HM. Analysis of a choke ring ground plane for multipath control in global positioning system (GPS) applications. IEEE Transactions on Antennas and Propagation. 1994;**42**:905-911